

Document Version

Final published version

Citation (APA)

Fan, J., Du, W., Chen, W., Chen, J., Gao, C., Zhang, L., Zhu, X., Ye, H., Chen, C., & Zhang, G. (2025). Enhanced hydrogen sulfide corrosion resistance of large-area sintered nano-copper for power electronics module using atmospheric pressure plasma jet treatment. *Applied Surface Science*, 713, Article 164263. <https://doi.org/10.1016/j.apsusc.2025.164263>

Important note

To cite this publication, please use the final published version (if applicable). Please check the document version above.

Copyright

In case the licence states "Dutch Copyright Act (Article 25fa)", this publication was made available Green Open Access via the TU Delft Institutional Repository pursuant to Dutch Copyright Act (Article 25fa, the Taverne amendment). This provision does not affect copyright ownership. Unless copyright is transferred by contract or statute, it remains with the copyright holder.

Sharing and reuse

Other than for strictly personal use, it is not permitted to download, forward or distribute the text or part of it, without the consent of the author(s) and/or copyright holder(s), unless the work is under an open content license such as Creative Commons.

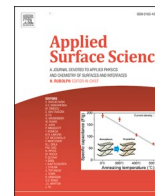
Takedown policy

Please contact us and provide details if you believe this document breaches copyrights. We will remove access to the work immediately and investigate your claim.

**Green Open Access added to [TU Delft Institutional Repository](#)
as part of the Taverne amendment.**

More information about this copyright law amendment
can be found at <https://www.openaccess.nl>.

Otherwise as indicated in the copyright section:
the publisher is the copyright holder of this work and the
author uses the Dutch legislation to make this work public.



Full Length Article

Enhanced hydrogen sulfide corrosion resistance of large-area sintered nano-copper for power electronics module using atmospheric pressure plasma jet treatment

Jiajie Fan^{a,b,c}, Wei Du^a, Wei Chen^{a,*}, Junwei Chen^a, Chenshan Gao^d, Liang Zhang^f, Xi Zhu^b, Huaiyu Ye^d, Chuan Chen^e, Guoqi Zhang^c

^a Shanghai Engineering Technology Research Center for SiC Power Device, College of Intelligent Robotics and Advanced Manufacturing, Fudan University, Shanghai 200433, China

^b Research Institute of Fudan University in Ningbo, Ningbo 315336, China

^c EEMCS Faculty, Delft University of Technology, Delft 2628, the Netherlands

^d Southern University of Science and Technology, Shenzhen 518000, China

^e State Key Laboratory of Environmental Adaptability for Industrial Products, China National Electric Apparatus Research Institute Co., Ltd, Guangzhou 510663, China

^f Changzhou Institute of Inspection Testing Standardization and Certification, Changzhou 213000, China

ARTICLE INFO

Keywords:

Sintered nanoCu
Atmospheric corrosion
Plasma jet
Corrosion protection
Density functional theory

ABSTRACT

In harsh offshore environments, large-area sintered nano-copper (Cu) interconnections, which serve as die attachment material or thermal interface material (TIM), are prone to degradation from hydrogen sulfide (H₂S) corrosion. This study introduced a film-forming technique based on atmospheric pressure plasma jet (APPJ) to improve the corrosion resistance of large-area sintered nanoCu joint. The corrosion protection mechanism against H₂S-containing atmospheric corrosion was investigated using both experimental methods and density functional theory (DFT) simulations. The key findings were as follows: (1) The deposition film, primarily composed of a Si-O₃ network, effectively protected sintered Cu plate from corrosion by H₂S gas, and maintaining the mechanical performance of sintered Cu joint after 384 h of H₂S testing. (2) The dissociation products of the APPJ-treated precursor hexamethyldisiloxane (HMDSO), -OSiCH₃ and -OSi(CH₃)₃, formed stable chemical bonds on the sintered nanoCu surface, resulting in the formation of -OSiCH₃(O-CH₃)₂ fragments. (3) The -OSiCH₃(O-CH₃)₂ fragments were unreactive toward to corrosion agents such as H₂S, O₂, and H₂O, and also serving as a barrier to block their access to the sintered nanoCu surface. This study provided a comprehensive understanding of the corrosion protection mechanism of sintered nanoCu using APPJ-deposited films, offering valuable insights for improving the reliability of power electronics.

1. Introduction

Traditional tin-based solders, with their low melting points, are insufficient to meet the high-temperature requirements of power electronics, particularly SiC-based devices [1–3]. As a result, sintered nanoCu, known for its “low-temperature processing and high-temperature service” characteristics, is often used as the interconnection material [4]. However, in corrosive environments like offshore settings with H₂S gas and salt mist, SiC power modules may experience excessive aging due to sintered nanoCu corrosion [5,6]. Therefore, improving the corrosion resistance of sintered nanoCu is essential for the

safe and reliable operation of next-generation SiC power modules in demanding environments like offshore wind power.

The unique climatic and chemical conditions in offshore environments accelerate the corrosion of sintered nanoCu [7,8]. These climatic environments are characterized by high temperatures, high humidity, and rapid fluctuations in both. The chemical conditions include corrosive factors such as salt mist and gases like H₂S and SO₂. Salt mist is produced by seawater collisions or evaporation [9]. Offshore oil and gas extraction also releases large quantities of H₂S, while the interaction between organic marine sediments and sulfate-reducing bacteria further contributes to H₂S release. In addition to offshore environments,

* Corresponding author at: Shanghai Engineering Technology Research Center for SiC Power Device, College of Intelligent Robotics and Advanced Manufacturing, Fudan University, Shanghai 200433, China.

E-mail address: chenw21@m.fudan.edu.cn (W. Chen).

<https://doi.org/10.1016/j.apsusc.2025.164263>

Received 13 May 2025; Received in revised form 12 July 2025; Accepted 4 August 2025

Available online 6 August 2025

0169-4332/© 2025 Elsevier B.V. All rights are reserved, including those for text and data mining, AI training, and similar technologies.

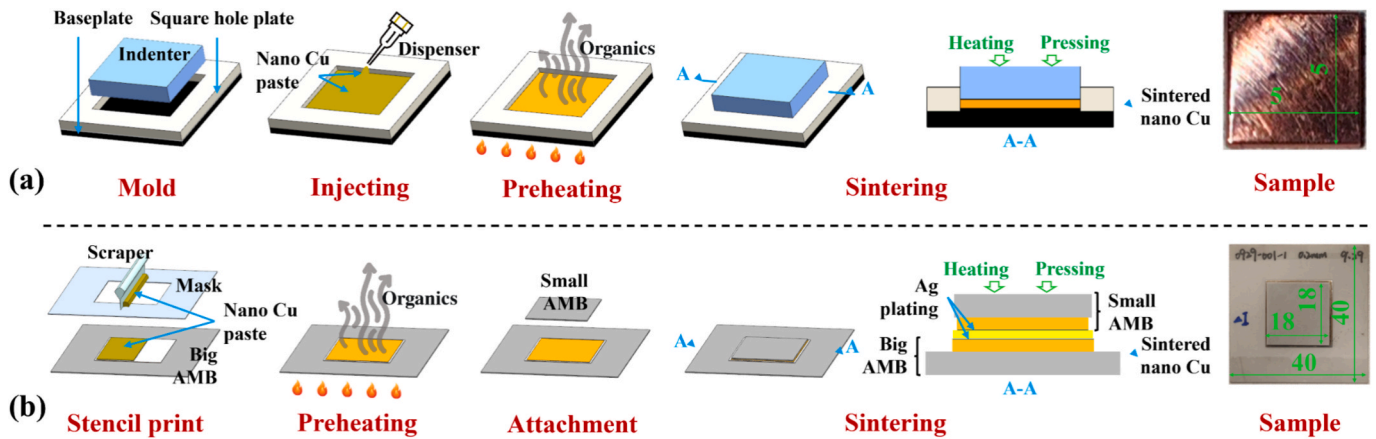


Fig. 1. Schematic of the sample preparation process: (a) sintered nanoCu plate, (b) sintered nanoCu joint.

sintered nanoCu are vulnerable to corrosion in other harsh settings, including hot springs, aquaculture facilities, fire smoke, humid climates, chemically polluted areas and so on [10,11].

Two main strategies are used to enhance the corrosion resistance of die interconnect materials: adding corrosion-resistant components and applying protective coatings. Common additives include organic compounds and nanoparticles. XY. Wang *et al.* [12] enhanced the corrosion resistance of sintered nanoCu by incorporating epoxy resin. This modification increased the open circuit potential in 3.5 % NaCl solution and improved resistance to H₂S-induced corrosion. D. Li *et al.* [13] enhanced the migration resistance of sintered nano Ag by adding nano-Si particles, with 0.1 % Si addition improving resistance by 6.3 times. D. Wang *et al.* [14] enhanced nano Ag's migration resistance by adding nano-sized Pd particles. Pd preferentially reacts with oxygen, reducing its availability for Ag oxidation. Additionally, Pd-Ag alloys and PdO serve as barriers to mitigate silver migration. D. Wang *et al.* [14] improved migration resistance in nano Ag by adding nano Pd particles, which form Pd-Ag alloys and PdO, inhibiting silver migration. C. Huang *et al.* [15] found that adding 0.3 wt% Ag₃Sn and Cu₃Sn nanoparticles to SAC305 solder reduced corrosion current and minimized surface corrosion. Y. Lv *et al.* [16] enhanced Sn-0.7Cu solder's corrosion resistance by adding nanographene sheets, refining grains and reducing the cathode area. SY. Tang *et al.* [17] found that adding nickel-coated carbon nanotubes to SnAgCu solder slightly improved corrosion resistance when the concentration was below 0.03 wt%, but decreased it when exceeding 0.05 wt%, leading to a rougher surface passivation film. However, few studies have focused on protective coatings. R. Riva *et al.* [18] deposited a 20 μm layer of parylene onto sintered Ag electrodes and alumina surfaces, effectively delaying Ag migration. HY. Tang *et al.* [19] developed Sn-enhanced PVB coatings and evaluated their anticorrosion performance on Cu substrates in 3.0 % NaCl using a three-electrode method. A 10-day corrosion test validated the coating's long-term effectiveness.

In recent years, atmospheric pressure low-temperature plasma (APPJ) technology has garnered increasing attention as an innovative surface treatment method due to its low temperature, energy efficiency, and environmental benefits [20–23]. Unlike traditional high-temperature processes, APPJ can induce physicochemical reactions without damaging the material substrate, thereby preventing thermal degradation. By adjusting treatment parameters such as power, duration, and gas composition, this technology can modify material surfaces, improving their properties and altering their microstructure. For example, functional films can be applied to enhance specific properties, including corrosion resistance, wettability, adhesion, antibacterial activity, and electrical conductivity [24–27]. As a result, APPJ technology shows great potential for widespread use in corrosion protection applications.

APPJ technology has proven effective in enhancing the corrosion

resistance of metal substrates through the deposition of various coatings. Studies have explored organic, nanoparticles and ceramic films as protective layers. PH. Li *et al.* [28] applied a hydrophobic polymer coating (2,2,3,4,4,4-hexafluorobutyl methacrylate) to improve the corrosion resistance of NiTi alloys. After APPJ treatment, the corrosion potential increased from -0.37 to -0.26 V, and the corrosion current significantly decreased. L. Silva *et al.* [29] used APPJ to deposit an organosilicon film on steel with hexamethyldisiloxane (HMDSO) as the polymerizing agent, reducing the corrosion current density from 1 to $0.00027 \mu\text{A}/\text{cm}^2$. C. Regula *et al.* [30] found that using a N₂-H₂ gas mixture in the APPJ process resulted in improved deposition quality compared to using compressed air. S. Halder *et al.* [31] deposited Fe-based amorphous powder on mild steel via APPJ, improving corrosion resistance, with a nonlinear relationship between enhancement and plasma power. ZJ. Wang *et al.* [32] exposed Ce metal to APPJ in air for 400 s, resulting in a dense 1 μm CeO₂ layer that effectively inhibited water adsorption and desorption. The layer remained stable under atmospheric conditions for 60 days without significant changes. KY. Lin *et al.* [33] used tetraethyl orthosilicate to deposit carbon-free SiO_x coatings on AZ91D magnesium alloy via APPJ, protecting it from Cl⁻ induced corrosion. After 14 days of immersion in a 3.5 % NaCl solution, no pitting was observed.

In recent years, plasma deposition technology has been widely used to improve the packaging performance of power modules, aiming to enhance both their overall performance and reliability. CY. Jiang *et al.* [34] applied plasma electrolytic oxidation (PEO) to form a dense Al₂O₃ ceramic layer on SiCp/Al substrates, thereby improving corrosion resistance, electrical insulation properties, and temperature stability. X. Zhu *et al.* [24] proposed a novel surface treatment method using precisely controlled micro APPJ to repair and enhance the electrical insulating properties of micro-metal defects at the Cu/epoxy resin interface in high-voltage power modules. YH. Shan *et al.* [35] studied the impact of APPJ-generated reactive species on the surface properties of three common polymer substrates in electronic packaging, offering insights for future chip packaging. Although APPJ shows potential for corrosion protection in electronic packaging, no evidence suggests it significantly improves the corrosion resistance of interconnect layers. Thus, developing an APPJ treatment system is crucial to explore its potential in this area.

This study proposes a method for depositing organic films on sintered nanoCu surfaces using APPJ, with HMDSO as the precursor. The physicochemical properties of the films and their corrosion resistance against NaCl solution and H₂S gas were experimentally validated. Additionally, density functional theory (DFT) simulations were used to analyse the adsorption behaviour of the films on sintered nanoCu surfaces and their mechanism in blocking corrosive agents. The manuscript is organized as follows: Section 2 describes the sample preparation and experimental setup, Section 3 examines the film properties, corrosion

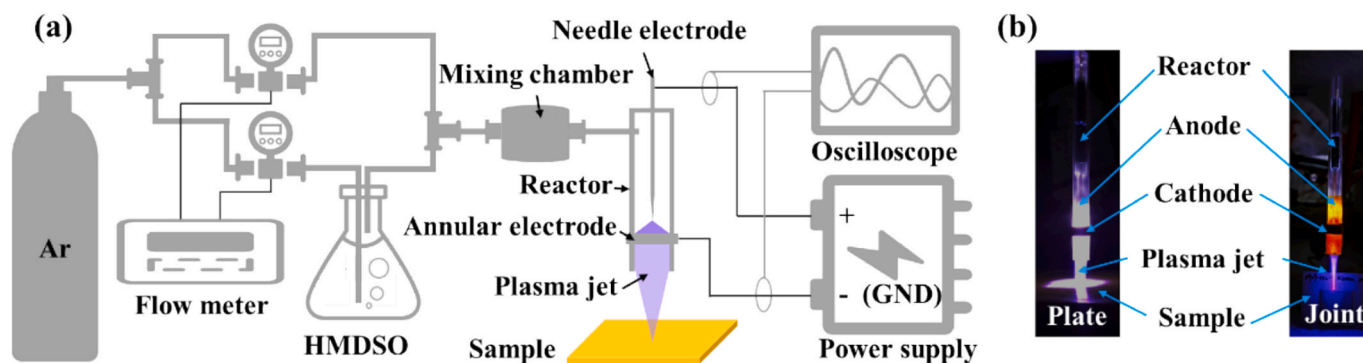


Fig. 2. (a) Schematic of the plasma surface modification platform and (b) discharge images for different samples.

protection, and mechanisms, and Section 4 provides the conclusions.

2. Experimental details

2.1. Sintered sample preparation

In this study, the corrosion and anticorrosion mechanisms of sintered nanoCu materials are investigated, involving two distinct samples: sintered nanoCu plate and sintered nanoCu joint, with the preparation process illustrated in Fig. 1. The Cu nanoparticle paste used consists of Cu nanoparticles with an average particle size ranging from 150 to 300 nm, along with ethylene glycol (99.5 %, from Aladdin Reagent Co., Ltd.) and terpinol (95.0 %, from Aladdin Reagent Co., Ltd.) [36]. The plate sample was fabricated using a self-designed square-shaped mold, while the joint sample was prepared using a stencil printing process [37]. Prior to sintering, the pre-coated paste was preheated at 120 °C for 30 min in a vacuum oven (DZF-6012, YIHENG) to remove the majority of the organic contaminants. The pressure-assisted sintering process was carried out in a nitrogen atmosphere using an industrial standard sintering machine (Sinterstar Innovate-F-XL, Boschman). For the plate sample, sintering was conducted at 250 °C and 20 MPa for 25 min, while for the joint sample, the sintering conditions were set at 250 °C and 20 MPa for 10 min.

The plate sample measures $5 \times 5 \times 1 \text{ mm}^3$. For the joint sample, two differently sized active metal brazing (AMB) substrates are connected using sintered nanoCu. The large AMB Si_3N_4 ceramic substrate measures $40 \times 40 \times 0.32 \text{ mm}^3$, with a brazed Cu layer measuring $19.4 \times 19.4 \times 0.32 \text{ mm}^3$ and a $0.6 \mu\text{m}$ Ag coating on the Cu surface. The small AMB Si_3N_4 ceramic substrate measures $18 \times 18 \times 0.32 \text{ mm}^3$, with a brazed Cu layer measuring $17.4 \times 17.4 \times 0.32 \text{ mm}^3$ and a $0.6 \mu\text{m}$ Ag coating on the Cu surface.

2.2. Film deposition method using APPJ

The sample surface film deposition system based on APPJ is shown in Fig. 2(a). An APPJ is generated using a needle-ring structure, which consists of a quartz glass tube as the reactor chamber, a high-voltage Cu needle as the positive electrode, and a Cu ring as the ground electrode. The reactor chamber dimensions are 8 mm in outer diameter, 6 mm in inner diameter, and 140 mm in length. The power supply operates with a voltage amplitude of 10 kV, a repetition frequency of 5 kHz, a pulse width of 1000 ns, and rising/falling edge durations of approximately 100 ns. The applied voltage and discharge current are monitored using an oscilloscope (Tektronix TDS2014B) equipped with a high-voltage probe (Tektronix P6015A) and a current coil (Pearson 4100).

One gas line uses high-purity argon (99.999 %) as the working gas, and the other uses hexamethyldisiloxane (HMDSO, Aladdin Biochemical Technology Co., Ltd., Shanghai, China) as the reactive medium, which is introduced via bubbling. The two gas flows are mixed and then directed into the APPJ reactor chamber. Gas flows are controlled by a mass flow

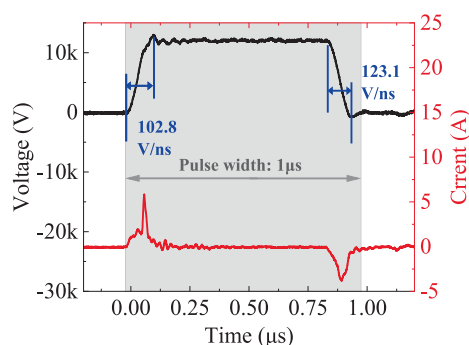


Fig. 3. The typical voltage and current waveforms within a single pulse.

controller (Sevenstar D07-19), with argon and HMDSO set at flow rates of 1500 ml/min and 35 ml/min, respectively. To achieve optimal film deposition, the distance between the reactor outlet and the sample surface is maintained at approximately 2 cm, as shown in Fig. 2(b). For both the plate and joint samples, the APPJ film deposition process lasted a total of 12 min, repeated four times, with each deposition lasting 3 min. During the deposition process, the distance between the reactor outlet and the sample surface was kept constant. The typical voltage and current waveforms under the conditions of 10 kV, a frequency of 5 kHz, and a pulse width of 1 μs are shown in Fig. 3.

2.3. Corrosion test

H_2S gas corrosion experiments were conducted to evaluate the effect of film deposition on the corrosion behavior of sintered nanoCu, which were conducted in a commercial gas corrosion chamber (GH-180, YAMASAKI), where sintered nanoCu plate samples, both with and without film deposition, were aged for 384 h in an H_2S environment at 45 °C, 85 % relative humidity, and 2 ppm H_2S concentration.

2.4. Characterization methods

The surface microstructure and elemental composition of the samples were analysed using scanning electron microscopy with energy-dispersive X-ray spectroscopy (SEM/EDS, SU8010, Hitachi). To determine the thickness of the deposited film and corrosion layer, cross-sectional cuts were made using a focused ion beam scanning electron microscope (FIB-SEM, Crossbeam 550, ZEISS), followed by observation and analysis. X-ray photoelectron spectroscopy (XPS, Axis Supra+, Shimadzu), with an Al $K\alpha$ excitation source ($h\nu = 1486.6 \text{ eV}$), was employed to analyse the chemical states of the elements in the deposited film. The surface mechanical properties of the samples were evaluated using nanoindentation testing (iNano, KLA). XPS spectra were processed using Thermo Advantage software.

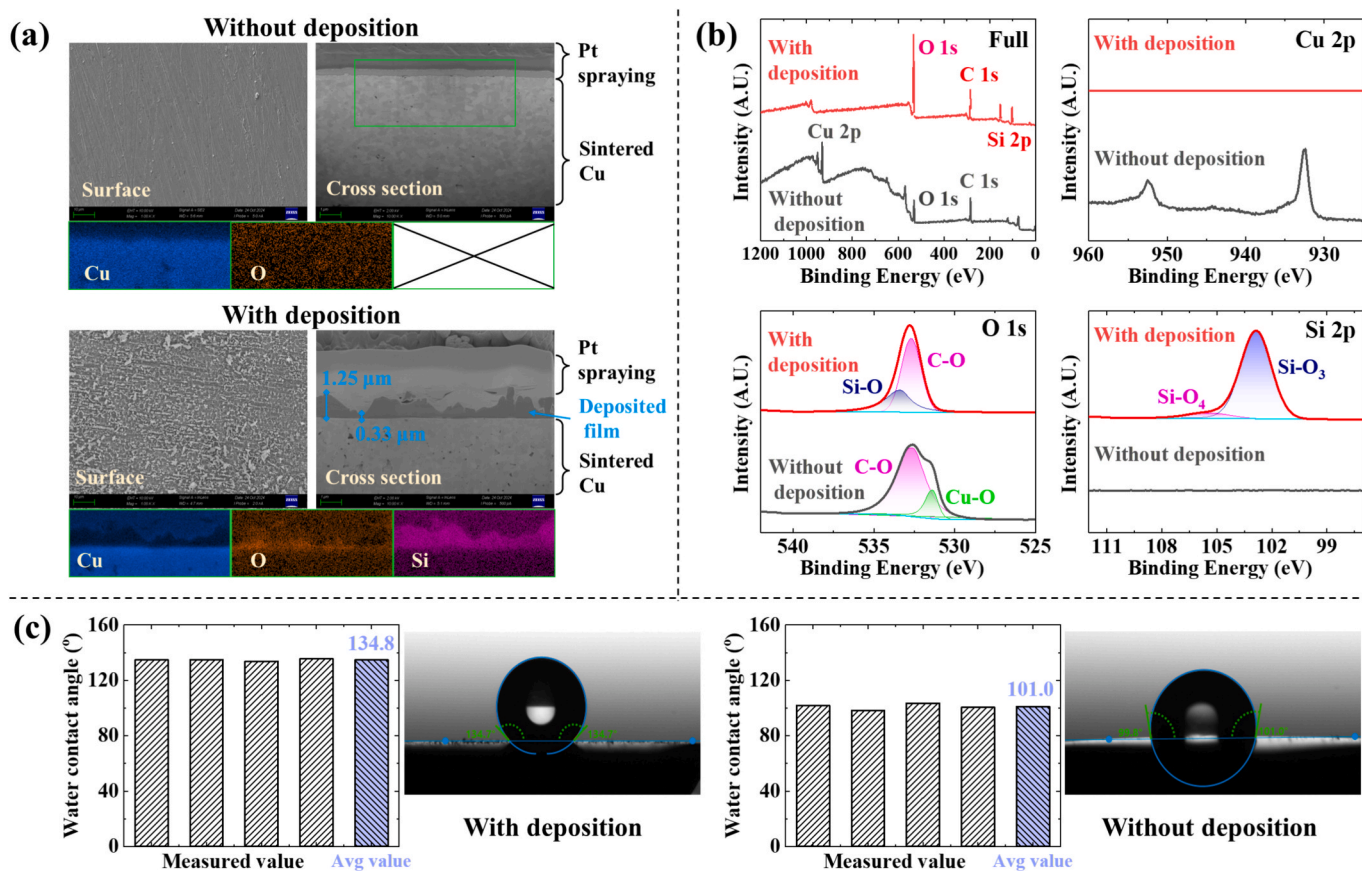


Fig. 4. (a) Surface and cross-sectional micromorphology, (b) surface chemical state, and (c) water contact angle measurements of the sintered nanoCu sample with and without deposition.

3. Results and discussion

In this section, the physical properties of the APPJ deposition film

were first analyzed. The corrosion protection of sintered nanoCu by the deposition film was then validated through gas corrosion experiments. Finally, DFT simulations were used to analyze the film formation process

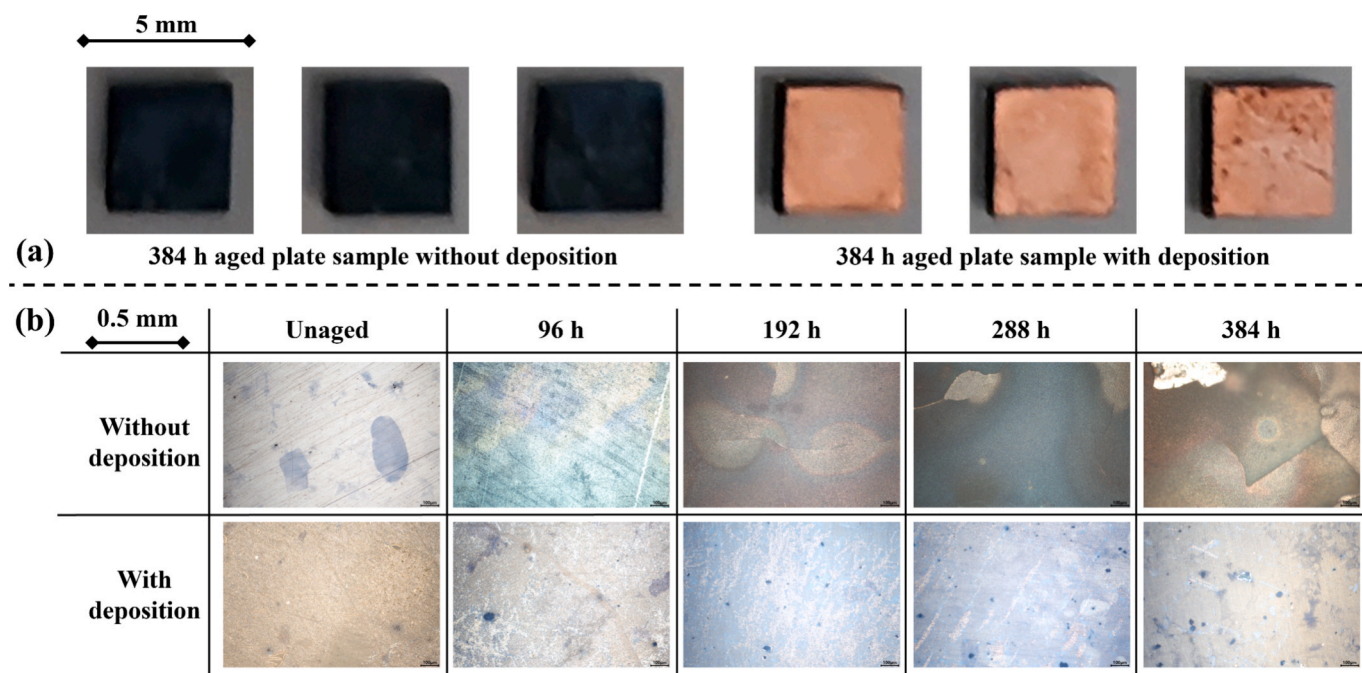


Fig. 5. (a) Macroscopic optical images of the plate samples surface with and without a deposition layer after 384 h of corrosion. (b) Microscopic optical images of the plate samples surface with and without a deposition layer at various corrosion times.

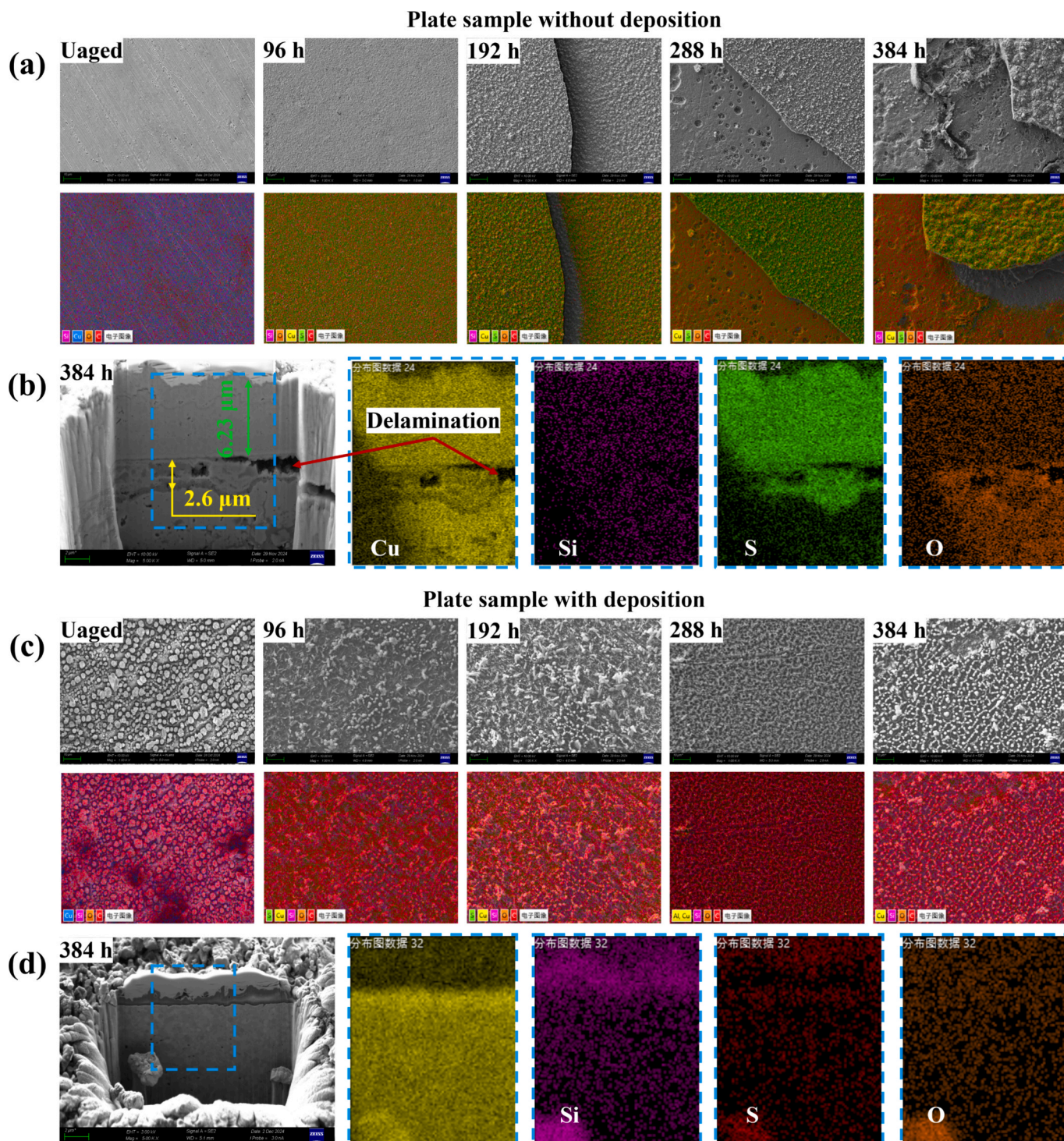


Fig. 6. Morphology and elemental composition characterization using SEM/EDS: (a) Surface features of the plate sample without deposition over increasing corrosion time; (b) Cross-sectional features of the 384 h aged plate sample without deposition; (c) Surface features of the plate sample with deposition over increasing corrosion time; (d) Cross-sectional features of the 384 h aged sintered nanoCu sample with deposition.

and its corrosion protection mechanism.

3.1. APPJ treatment analysis

To analyze the physical state and elemental composition of the deposited film, surface and cross-sectional analyses were performed on the sintered samples, both with and without deposition. The results were shown in Fig. 4(a). The original plate sample had a relatively flat surface, but after APPJ treatment, the sintered nanoCu sample developed a

typical particle-clustered film, which significantly increased the surface roughness. Cross-sectional observations revealed that the bottom layer of the film consisted of interpressed and crosslinked spherical particles, forming a dense structure. The film exhibited a wavy morphology, indicating vertical growth during plasma deposition, with a thickness ranging from 0.33 to 1.25 μm. EDS surface scan results indicated that the deposited APPJ film primarily consisted of Si and O elements. XPS analysis of the film’s detailed chemical state was subsequently conducted, as shown in Fig. 4(b). Since no Cu element was detected in the

Table 1

Surface molecular weight percentage of each element in the EDS scanning region for samples with and without deposition under different aging times.

Sample type	Aging time/h	Cu/at %	O/at %	S/at %	Si/at %	C/at %
Plate sample without deposition	0	72.69	5.09	0	0	22.21
	96	47.03	2.24	26.8	0	23.93
	192	39.64	1.65	34.48	0	24.23
	288	43.35	14.8	20.54	0	21.31
384	44.97	20.39	14.17	0	20.47	
Plate sample with deposition	0	0.61	40.26	0	33.11	26.02
	96	2.05	45.88	0	29.57	22.5
	192	1.3	50.78	0	32.62	15.3
	288	2.11	55.96	0	30.11	11.83
	384	0.76	40.27	0	32.61	26.37

Table 2

Cross-sectional molecular weight percentage of each element in the EDS scanning region for 384 h aged samples with and without deposition.

Sample type	Aging time/h	Cu/at %	O/at %	S/at %	Si/at %	C/at %
Without deposition	384	46.4	11.3	31.5	0	10.8
With deposition	384	54.9	9.3	1	18	16.9

full spectrum of the plate sample with deposition, it confirmed that the deposited film completely covered the surface of the sintered nanoCu. The Si 2p spectrum was divided into two chemical states based on the number of Si atoms bonded to O atoms. The peak at 102.84 eV corresponded to $-\text{Si-O}_3$, while the peak at 105.32 eV corresponded to $-\text{Si-O}_4$ [38], with a $-\text{Si-O}_3$ to $-\text{Si-O}_4$ ratio of 92 % to 8 %. The deposited film exhibited a higher degree of cross-linked polymerization due to a higher number of O atoms bonded to Si atoms. For the sintered nanoCu sample without deposition, the surface was mainly composed of Cu and Cu oxides. Fig. 4(c) illustrated the water contact angles (WCA) and water droplet images on the surface of the sintered nanoCu samples, both without and with deposition, showing average contact angles of 101.0° and 134.8° , respectively. After APPJ deposition, the hydrophobicity of the sintered nanoCu sample increased significantly by ~ 33 %.

3.2. Corrosion test result analysis

During the 384 h H_2S gas corrosion experiment, sintered plate samples, both with and without deposition, were collected at 96 h intervals. Fig. 5(a) shows the macroscopic optical images of plate surfaces with and without a deposition layer after 384 h of corrosion aging. The surface of the sample without a deposition layer darkened significantly, while the sample with a deposition layer retained its original colour. Fig. 5(b) shows the microscopic optical images of sample surfaces at different aging time. Over the 384 h corrosion period, samples without the deposition exhibited a progressive accumulation of corrosion

products, which eventually cracked and detached. In contrast, samples with the deposition maintained an intact film throughout the aging process, effectively protecting the surfaces and preventing visible corrosion product formation.

The surface morphology of samples under different aging times and the cross-sectional morphology of 384 h aged samples, both with and without deposition, were analysed using SEM/EDS technology, as shown in Fig. 6. The elemental compositions of their surfaces and cross-sections are summarized in Tables 1 and 2, respectively. For the sintered sample without deposition, a layered corrosion product formed in a 2 ppm H_2S atmosphere, as shown in Fig. 6(a). As the corrosion product accumulated on the sample's surface, the layers experienced cracking (around 192 h), detachment (around 288 h), and continued growth of the corrosion layer on the newly exposed substrate (around 384 h). Notably, once cracks appeared in the corrosion product layer, H_2S gas penetrated and reacted with the underlying sintered nanoCu material. The cross-sectional view of the 384 h aged sintered sample without deposition was prepared using FIB, as shown in Fig. 6(b). A corrosion product film, approximately $6.23 \mu\text{m}$ thick, was observed on the surface, which had separated from the underlying sintered nanoCu substrate. Corrosive gases penetrated through gaps in the upper corrosion film, reacted with the substrate beneath, and caused further damage. The corrosion depth of the substrate was measured to be approximately $3 \mu\text{m}$. In our previous research, we found that the corrosion products were primarily composed of Cu_2O , Cu_2S , CuO , and CuS [5,6]. For the sintered sample with deposition, Fig. 6(c) illustrates the surface features over increasing aging time. Throughout the corrosion process, no alterations were observed in the deposited film, which retained its original state. EDS analysis showed no S presence on the surface of the deposited film, confirming that the APPJ-deposited film did not interact with H_2S under the experimental conditions of this study. Fig. 6(d) presents the cross-sectional features of the sintered sample aged for 384 h. The deposited film remained intact and tightly bonded to the sintered nanoCu surface. Furthermore, no S element was detected in the cross-section, which further demonstrated that the APPJ-deposited film effectively resisted corrosion from H_2S , O_2 , and other environmental corrosive agents.

A cluster-like protrusion appeared on the surface of the 384 h aged sintered sample with deposition, as shown in Fig. 7(a). EDS surface scanning analysis revealed that the APPJ-deposited film was compromised, showing a significant absence of Si and O elements in this region. In contrast, Cu and O elements were noticeably present in this region. Cross-sectional analysis of this region was conducted, as shown in Fig. 7(b). The image reveals that the APPJ-deposited film was absent in the center of the protrusion and had detached from the sintered nanoCu surface. Below the missing film region, radial corrosion had penetrated into the sintered nanoCu substrate. Above this region, a significant accumulation of corrosion products had occurred. The protrusions observed on the surface of the 384 h aged sintered sample are infrequent, suggesting that these defects might originate from the APPJ film deposition process. Future research should focus on optimizing the APPJ deposition method, including adjustments to the plasma jet reactor, capillary structure, and control of gas flow rate and excitation source parameters, to improve the quality of the deposited film.

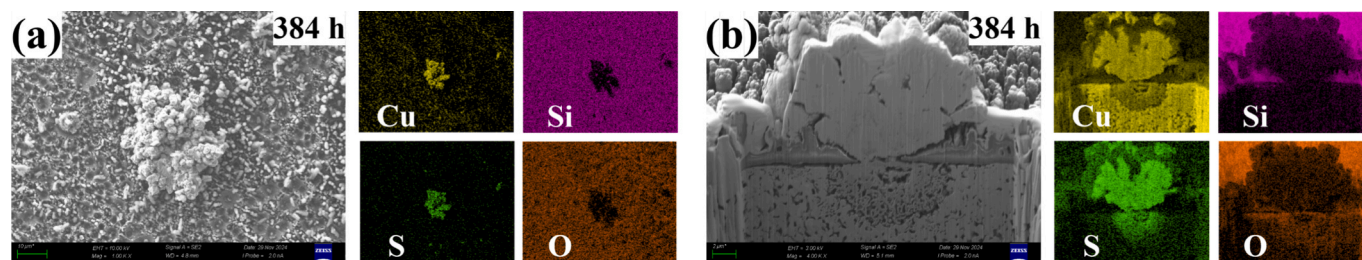


Fig. 7. Characterization of (a) surface and (b) cross-sectional morphology and elemental composition in the defect regions of the APPJ-deposited film after 384 h of corrosion aging.

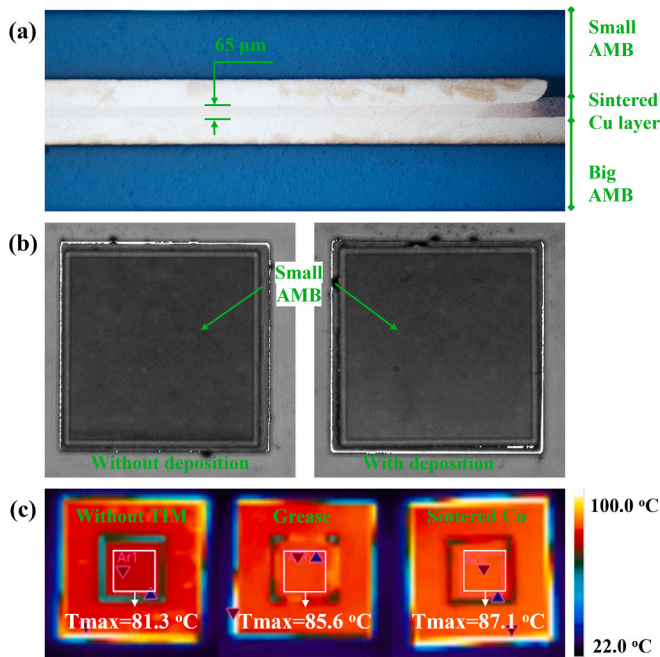


Fig. 8. (a) Cross-section, (b) SAT image, and (c) thermal performance evaluation of the joint sample.

3.3. Interconnect performance analysis

3.3.1. Sintering performance analysis

Sintered nanoCu can serve as a die attachment material to connect chips to substrates, as well as a thermal interface material (TIM) for linking electronic packages to heat dissipation systems. When used as a TIM, sintered nanoCu is exposed to the external environment without the protection of encapsulation materials, making it more susceptible to corrosion. Therefore, large-area sintered nanoCu joint sample used as TIM will be investigated in this study to evaluate the enhancement of corrosion resistance through APPJ deposited films. In the joint sample, the small AMB simulates the package, while the large AMB represents the heat sink.

The joint sample image is shown in Fig. 1(b). To assess the performance of the interconnection layer, the joint sample's cross-section was prepared using metallographic techniques, including cold mounting, cutting, grinding, and polishing. As illustrated in Fig. 8(a), the cross-sectional analysis reveals that the sintered nanoCu layer, with a bond-line thickness (BLT) of approximately 65 μm, effectively bonded the two AMB pieces. No delamination, cracks, or noticeable holes were observed. Additionally, T-mode SAT was employed to further evaluate the interconnection performance, and the results are displayed in Fig. 8 (b). The SAT images confirm the absence of significant holes or delamination within the interconnection layer, demonstrating the high quality of the interconnection.

High thermal performance is essential for TIM. The heat transfer performance of three different TIMs was compared: no TIM, thermal grease (thermal conductivity of 6.2 W/m-K, 7868, Shin-Etsu), and sintered nanoCu. The samples were placed on a temperature-controlled plate set to 100 °C for 5 min to achieve thermal equilibrium, after which the maximum surface temperature of the small AMB was measured using an infrared camera. A higher surface temperature indicates better thermal transfer performance. The highest surface temperatures for the small AMB in the no TIM, thermal grease, and sintered nanoCu samples were 81.3 °C, 85.6 °C, and 87.1 °C, respectively. Compared to the no TIM and thermal grease samples, the sintered nanoCu sample exhibited improvements in thermal performance of 31.0% and 10.4%, respectively.

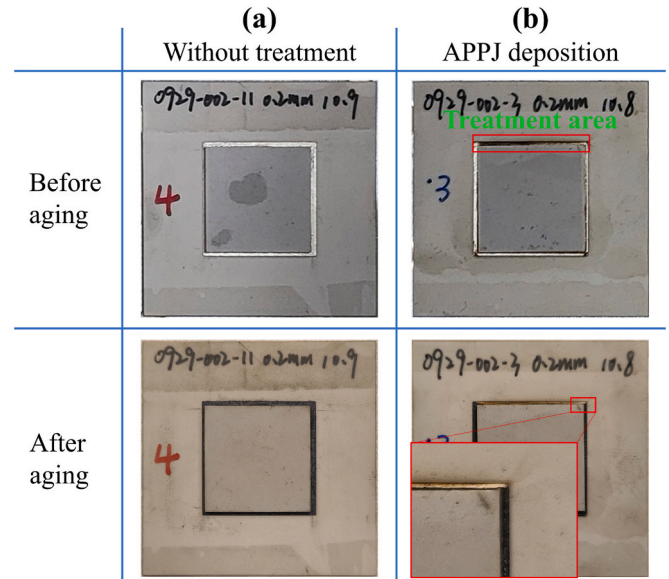


Fig. 9. Optical photos of sintered nanoCu joint samples before and after aging: (a) untreated sample; (b) APPJ film deposited sample.

3.3.2. Corrosion resistance analysis

To improve the corrosion resistance of the joints, an APPJ film was deposited on the overflow region of the sintered nanoCu material of the joint sample. As illustrated in Fig. 9(b), the film was applied to only one side of the overflow area. Subsequently, a 384 h 2 ppm H₂S gas corrosion test was performed on joint samples both with and without the film deposition, with the pre- and post-corrosion images shown in Fig. 9. The results revealed that the bare metal areas on the non-deposited sample including the exposed AMB silver layer and the sintered nanoCu layer, were entirely corroded to a black colour, whereas the film-deposited region showed no significant discoloration. This confirms that the APPJ-deposited film provides effective protection against corrosive agent in the environment.

To assess the impact of H₂S corrosion on material properties, cross-sectional joint samples with and without film deposition were prepared using metallographic embedding, cutting, grinding, and polishing techniques. Nanoindentation tests were subsequently conducted on the sintered nanoCu region of the cross-section to determine the elastic modulus (*E*) and hardness (*H*) of the interconnect layer. The spacing between adjacent indentations was maintained at 30 μm in both the x and y directions. All tests were carried out according to ISO 14577, employing a load of 50 mN, a loading rate of 5 mN/s, and a hold time of 1 s. Fig. 10 present the distributions of *E* and *H* across the sintered nanoCu layer of the joint sample. The overflow width was measured to be approximately 100 μm. Owing to the absence of applied pressure during sintering, the *E* and *H* values in the overflow region of the sintered nanoCu were relatively low; however, moving from the overflow region to the edge of the interconnect layer, these values progressively increased and reached a stable level.

To clearly compare the variations in the *E* and *H* of the sintered nanoCu layer in joint samples before and after H₂S corrosion aging, average *E* and *H* values were calculated at different positions (see Fig. 11). The data reveal that, from the edge of the sintered nanoCu extending approximately 300 μm into the interconnect layer, both *E* and *H* gradually increase to a maximum value. Beyond this distance, the values stabilize with only minor fluctuations. Specifically, the stable average *E* values for the unaged sample, the aged joint sample with deposition, and the aged joint sample without deposition were 160.85, 161.72, and 142.05, respectively. Compared to the unaged sample, the *E* value remained essentially unchanged in the aged sample with film deposition, whereas it decreased by approximately 11 % in the aged

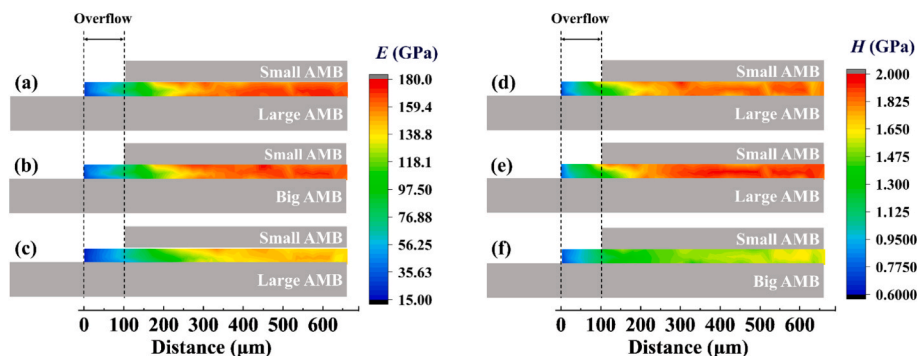


Fig. 10. Elastic modulus distribution of (a) unaged joint samples and 384 h 2 ppm H_2S aged joint samples (b) with and (c) without deposition; Hardness distribution of (d) unaged joint samples, 384 h 2 ppm H_2S aged joint samples, and within the aged group, (e) with and (f) without deposition.

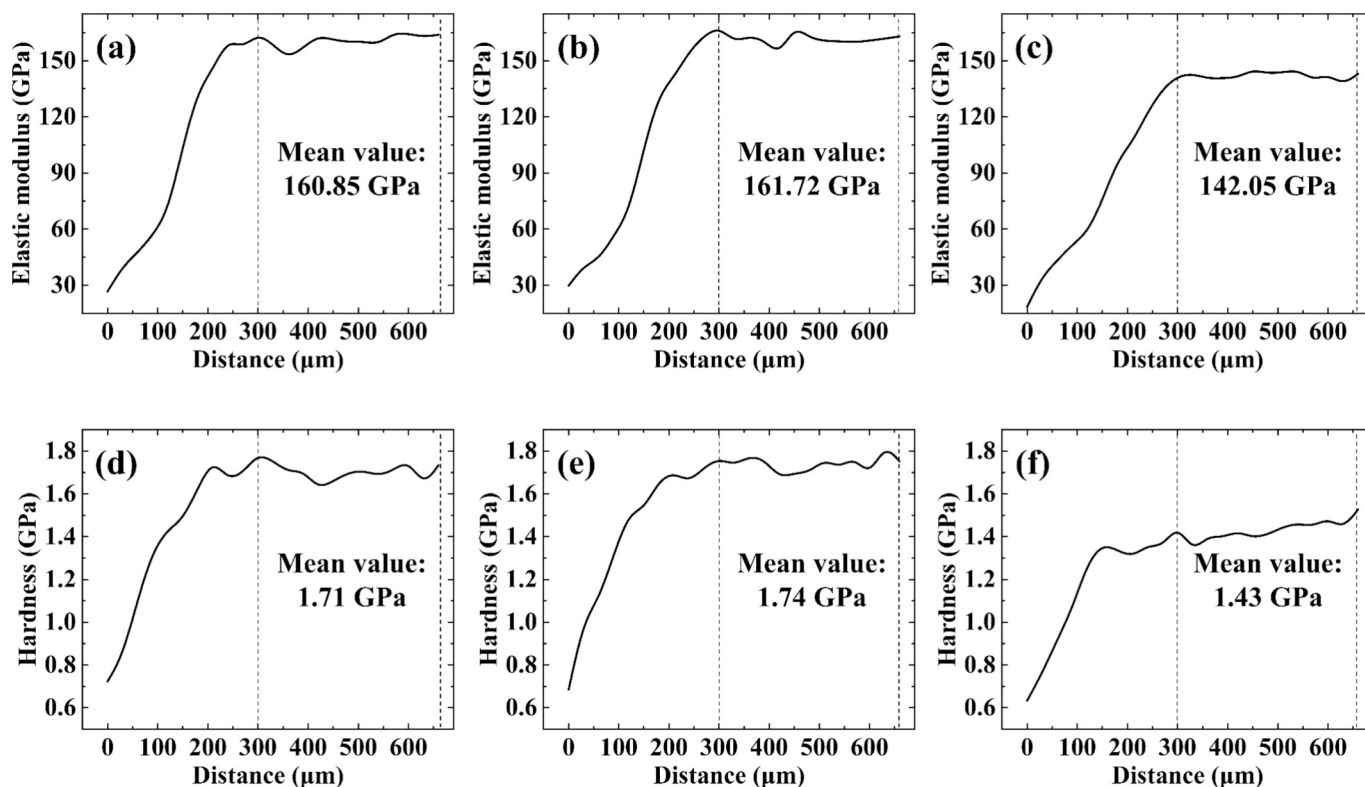


Fig. 11. Variation in average elastic modulus as a function of depth into the interconnect layer for (a) unaged joint samples and 384 h 2 ppm H_2S aged joint samples with (b) and without (c) film deposition. Variation in average hardness as a function of depth into the interconnect layer for (d) unaged joint samples and 384 h 2 ppm H_2S aged joint samples with (e) and without (f) film deposition.

sample without film deposition. Similarly, the stable average H values were 1.71, 1.74, and 1.43 GPa for the unaged, deposited aged, and undeposited aged joint samples, respectively; the H value of the aged joint sample with deposition was nearly the same as that of the unaged sample, while that of the aged joint sample without deposition declined by roughly 16%. This comparison further substantiates that the APPJ-deposited film provides effective corrosion protection for the sintered nanoCu joints during the corrosion aging process.

3.4. Corrosion resistance mechanism analysis

This section investigated the formation of plasma-deposited films and their role in improving the corrosion resistance of sintered nanoCu through simulation methods. DFT method was used to examine the interactions between atoms, molecules, and organic fragments, with simulations performed using Materials Studio software (Accelrys, Inc.).

The generalized gradient approximation (GGA) exchange–correlation functional, along with the Perdew–Burke–Ernzerhof (PBE) method, was used to describe the electron–electron interactions. The system’s wavefunction was represented using the double numerical with polarization (DNP) basis set, as defined in the basis file 4.4. The calculations were performed with an electronic self-consistent field (SCF) convergence threshold set to 0.00005 eV and a smearing value of 0.005 Ha to facilitate SCF convergence. Additionally, the energy convergence tolerance, maximum force, and maximum displacement were set to 0.00002 Ha, 0.004 Ha/Å, and 0.005 Å, respectively.

3.4.1. Film deposition process

The dissociation of covalent bonds such as Si–O and Si–C allows HMDSO molecules to break into fragments like $-OSi(CH_3)_3$, $-OSi(CH_3)_2$, $-OSiCH_3$, $-OSi$, and $-CH_3$ in the high-energy plasma jet. As shown in Fig. 12(a), the Gibbs free energy (ΔG) for the dissociation of

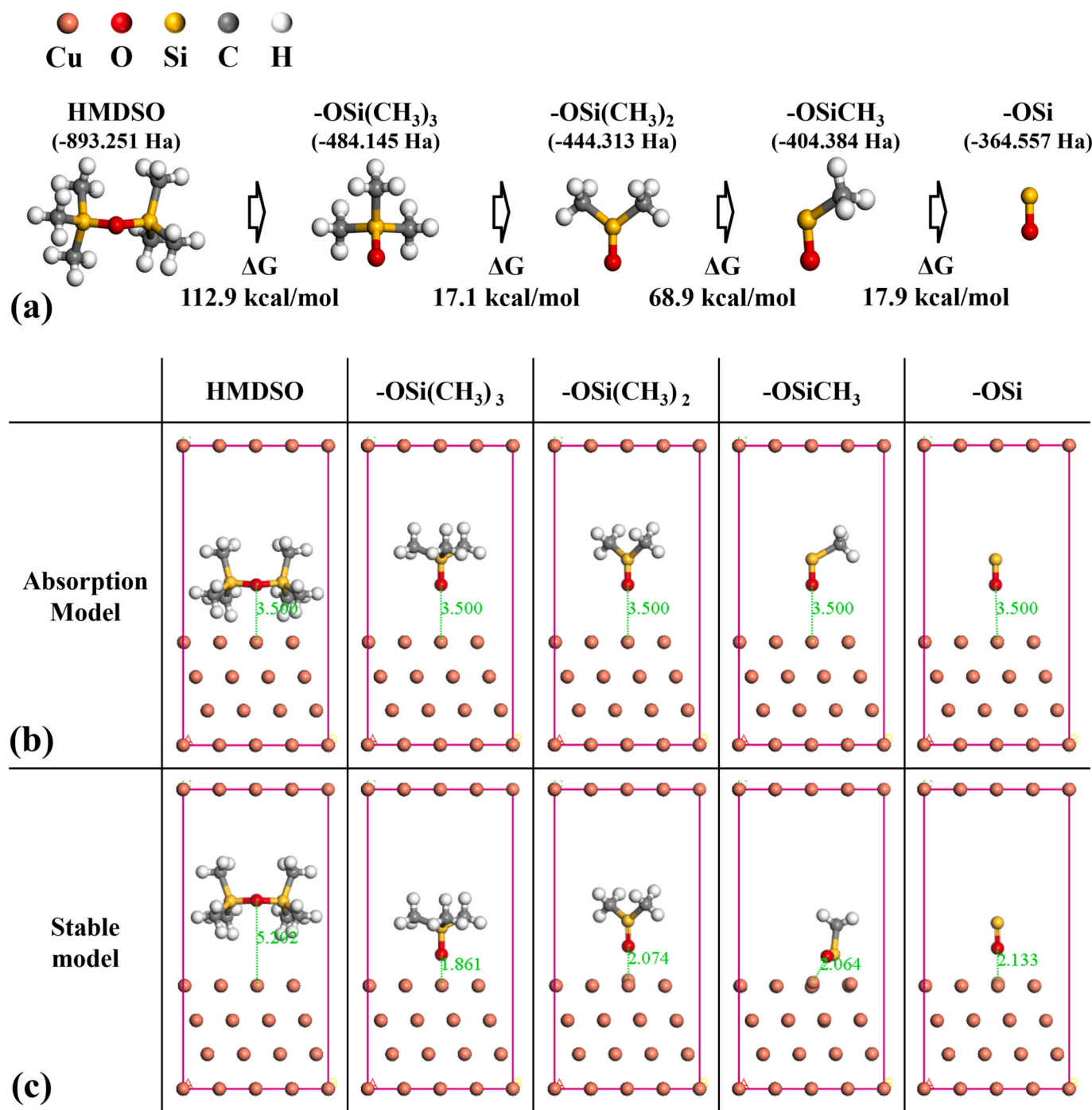


Fig. 12. (a) Dissociation pathways of HMDSO into various fragments, (b) Adsorption model of HMDSO and its dissociated fragments on the Cu(1 1 1) surface, and (c) Stable model after energy optimization.

HMDSO into $-\text{OSi}(\text{CH}_3)_3$, $-\text{OSi}(\text{CH}_3)_3$ into $-\text{OSi}(\text{CH}_3)_2$, $-\text{OSi}(\text{CH}_3)_2$ into $-\text{OSiCH}_3$, and $-\text{OSiCH}_3$ into $-\text{OSi}$ are 112.9, 17.1, 68.9, and 17.9 kcal/mol, respectively [39]. Since the ΔG values for all these processes are positive, dissociation cannot occur spontaneously. Therefore, the decomposition depends on the energy supplied by the plasma. It is important to note that the breakdown of HMDSO does not follow a stepwise sequence. Under APPJ treatment, various decomposition processes can occur concurrently.

HMDSO and its dissociated fragments were directed by an Ar gas flow and deposited onto the surface of the sintered nanoCu sample. To investigate the film formation process, a model was constructed to simulate the adsorption of HMDSO and its dissociated fragments on the

Cu(1 1 1) surface, as illustrated in Fig. 12(b). Previous studies showed that the Cu(1 1 1) surface exhibited a notably low surface free energy, indicating high stability [40]. As a result, the Cu(1 1 1) surface was commonly selected as an ideal model for studying stability, structure, and adsorption properties. In this study, the Cu(1 1 1) surface was modeled using a five-layer slab derived from a (5×5) supercell to investigate HMDSO adsorption. In all adsorption models, the O atom in HMDSO and its dissociated fragments was positioned directly above the central Cu atom on the Cu(1 1 1) surface, at a distance of 3.5 Å. After geometry optimization, the lowest-energy structure of each model was obtained, as shown in Fig. 12(c). For the adsorption models of HMDSO, $-\text{OSi}(\text{CH}_3)_3$, $-\text{OSi}(\text{CH}_3)_2$, $-\text{OSiCH}_3$, and $-\text{OSi}$, the distance between Cu

Table 3The E_{ads} values and d_{Cu-O} values for five adsorption systems.

Adsorption system	E_{ads} (eV)	$d_{adsorbate-metal}$ (Å)
HMDSO on Cu(1 1 1)	-1.34	5.202
-OSi(CH ₃) ₃ on Cu(1 1 1)	-2.59	1.861
-OSi(CH ₃) ₂ on Cu(1 1 1)	-1.59	2.074
-OSiCH ₃ on Cu(1 1 1)	-2.91	2.064
-OSi on Cu(1 1 1)	-1.25	2.133

and O (d_{Cu-O}) changed from 3.5 Å to 5.202, 1.861, 2.074, 2.064, and 2.133 Å, respectively. The variation in the d_{Cu-O} indicates the adsorption strength and stability between the adsorbates and the Cu(1 1 1) surface. In the HMDSO adsorption model, a large d_{Cu-O} (5.202 Å) indicates a weaker interaction, making it less likely to form a stable chemical bond. In contrast, the smaller d_{Cu-O} values suggest stronger interactions between the dissociated fragments of HMDSO and Cu(1 1 1).

To further verify the type of adsorption between HMDSO, its dissociated fragments, and Cu(1 1 1), the adsorption energy (E_{ads}) was calculated using the following equation:

$$E_{ads} = E_{slab+adsorbate} - E_{slab} - E_{adsorbate} \quad (1)$$

where $E_{adsorbate+slab}$ is the total energy of the relaxed adsorbate–surface system, and E_{slab} and $E_{adsorbate}$ are the total energies of the relaxed Cu(1 1 1) surface and the adsorbate. The E_{ads} values for the five adsorption systems are shown in Table 3. Adsorption energy directly affects stability, with chemisorption typically having lower values. Among the models, -OSiCH₃ showed the strongest adsorption energy (-2.91 eV) and the shorter d_{Cu-O} (2.064 Å), indicating it is the most stable. -OSi(CH₃)₃ had an adsorption energy of -2.59 eV, slightly weaker than -OSiCH₃. The adsorption modes of -OSiCH₃ and -OSi(CH₃)₃ are likely to be chemisorption.

During the APPJ treatment, -OSiCH₃ and OSi(CH₃)₃ were continuously deposited and crosslinked to form a deposition film primarily composed of -Si-O₃ [confirmed in Fig. 4(b)]. The film formation process is shown in Fig. 13. For -OSiCH₃, the O atom formed a chemisorptive bond with the surface Cu atoms. The unsaturated Si atoms then reacted with excited O atoms from the air to form covalent bonds. Subsequently, the unsaturated O atoms combined with the dissociated -CH₃ groups, resulting in the Cu-OSiCH₃(O-CH₃)₂ structure. For -OSi(CH₃)₃, the O atom also formed a chemisorptive bond with the Cu surface. Two -CH₃ groups were dissociated from -OSi(CH₃)₃ by APPJ energy, after which the unsaturated Si atoms reacted with excited O atoms from the air.

Finally, the unsaturated O atoms reacted with the dissociated -CH₃ groups, forming the Cu-OSiCH₃(O-CH₃)₂ structure.

3.4.2. Corrosion resistance analysis

In H₂S gas corrosion, H₂O, H₂S and O₂ in the environment can corrode sintered nanoCu samples. The adsorption behaviours of H₂O, OH, H₂S, S, O₂, and O on Cu(1 1 1) and -OSiCH₃(O-CH₃)₂ models were investigated, the results are showed in Fig. 14. In the H₂O-OSiCH₃(O-CH₃)₂ and OH-OSiCH₃(O-CH₃)₂ models, the H₂O or OH molecules were oriented parallel to Cu(1 1 1), with the O atom positioned directly above the C atom in the CH₃ group of -OSiCH₃(O-CH₃)₂, at a distance of 3.5 Å. In the H₂O-Cu(1 1 1) and OH-Cu(1 1 1) models, the O atom in H₂O or OH was directly above the Cu atom at the center of the Cu(1 1 1) surface, also at a distance of 3.5 Å. The adsorption and stable models are shown in Fig. 14(a), and the E_{ads} along with the distances between the adsorbate and the surface ($d_{adsorbate-surface}$) are listed in Table 4. After geometry optimization to the lowest energy, the $d_{adsorbate-surface}$ values for the H₂O-OSiCH₃(O-CH₃)₂, H₂O-Cu(1 1 1), OH-OSiCH₃(O-CH₃)₂, and OH-Cu(1 1 1) models changed from 3.5 Å to 4.357, 2.456, 3.061, and 2.037 Å, respectively, with corresponding E_{ads} values of -0.35, -0.43, -1.26, and -3.81 eV. The interactions between H₂O and Cu(1 1 1), as well as those between H₂O and -OSi(CH₃)₂(O-CH₃)₂, were relatively weak. While OH could only stably adsorb on the Cu(1 1 1) surface, it exhibited a weaker interaction with -OSi(CH₃)₂(O-CH₃)₂.

In the H₂S-OSiCH₃(O-CH₃)₂ and S-OSiCH₃(O-CH₃)₂ models, the S atom was positioned 3.5 Å above the C atom in CH₃ group of -OSiCH₃(O-CH₃)₂. In the H₂S-Cu(1 1 1) and S-Cu(1 1 1) models, the S atom was placed 3.5 Å above the Cu atom at the Cu(1 1 1) surface center. Fig. 14(b) shows the adsorption and stable models, with E_{ads} and $d_{adsorbate-surface}$ in Table 4. After geometry optimization, the $d_{adsorbate-surface}$ values for the H₂S-OSiCH₃(O-CH₃)₂, H₂S-Cu(1 1 1), S-OSiCH₃(O-CH₃)₂, and S-Cu(1 1 1) models changed to 4.652, 2.586, 3.679, and 2.245 Å, respectively, with E_{ads} of -0.44, -0.40, -1.12, and -5.24 eV. The analysis shows that no strong interaction occurred between adsorbates and surface atoms in the H₂S-OSiCH₃(O-CH₃)₂, H₂S-Cu(1 1 1), and S-OSiCH₃(O-CH₃)₂ models. Only in the S-Cu(1 1 1) model did the S atom stably adsorb onto the Cu(1 1 1) surface. Other studies confirmed that H₂S dissociated into S, which was adsorbed by Cu(1 1 1) [41,42].

In the O₂-OSiCH₃(O-CH₃)₂ and O-OSiCH₃(O-CH₃)₂ models, the O atom was positioned 3.5 Å above the C atom in the CH₃ group of -OSiCH₃(O-CH₃)₂. In the O₂-Cu(1 1 1) and O-Cu(1 1 1) models, the O atom was located 3.5 Å above the Cu atom at the center of the Cu(1 1 1) surface. Fig. 14(c) shows the adsorption and stable models, with the E_{ads}

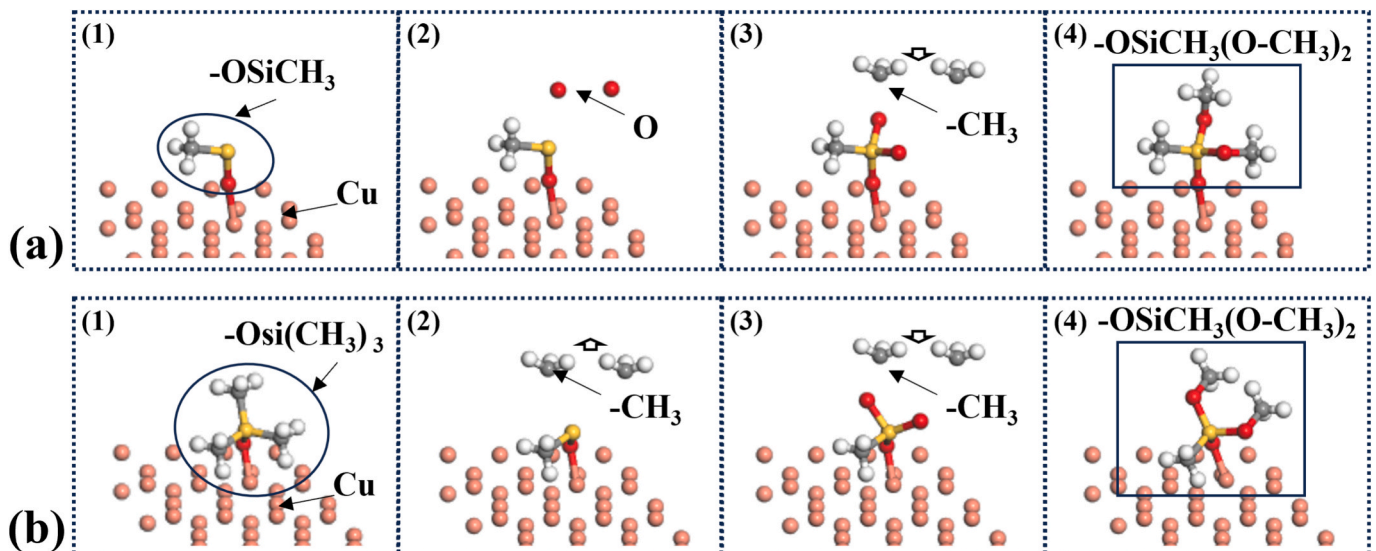


Fig. 13. The formation pathways of the APPJ deposition film (-OSiCH₃(O-CH₃)₂): (a) from -OSiCH₃; (b) from OSi(CH₃)₃.

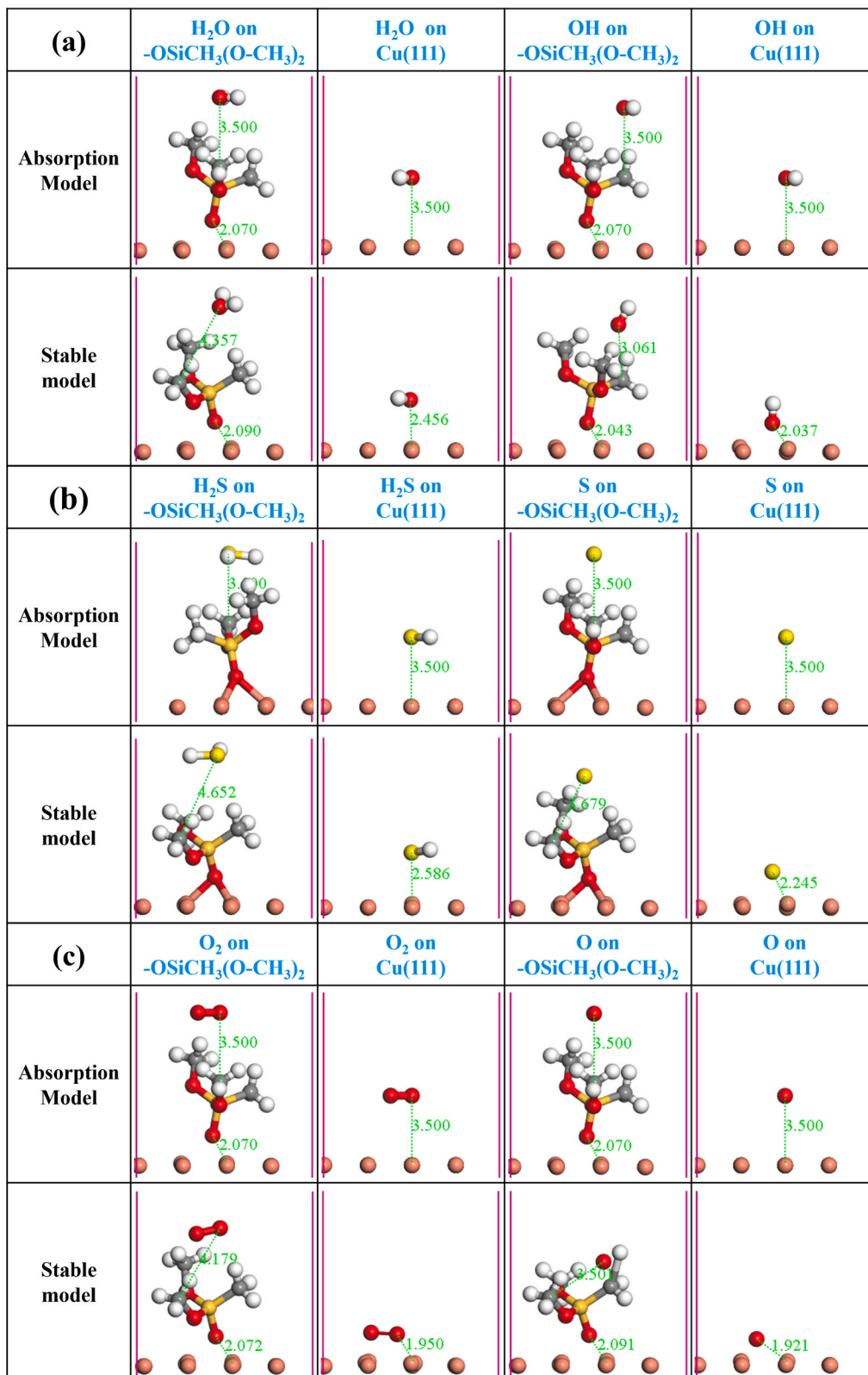


Fig. 14. Possible adsorption behaviours of sintered nanoCu, with and without deposition, in H₂S-containing atmospheric environment: (a) adsorption of H₂O and dissociated of OH on Cu (1 1 1) and -OSiCH₃(O-CH₃)₂; (b) adsorption of H₂S and dissociated of S on Cu (1 1 1) and -OSiCH₃(O-CH₃)₂; (c) adsorption of O₂ and dissociated of O on Cu (1 1 1) and -OSiCH₃(O-CH₃)₂.

Table 4

The E_{ads} values and the distances between the adsorbate and the surface ($d_{adsorbate-surface}$) for the stable systems.

Adsorption system	$E_{ads}(eV)$	$d_{adsorbate-surface}(\text{\AA})$
H ₂ O on -OSiCH ₃ (O-CH ₃) ₂	-0.35	4.357
H ₂ O on Cu(1 1 1)	-0.43	2.456
OH on -OSiCH ₃ (O-CH ₃) ₂	-1.26	3.061
OH on Cu(1 1 1)	-3.81	2.037
H ₂ S on -OSiCH ₃ (O-CH ₃) ₂	-0.44	4.652
H ₂ S on Cu(1 1 1)	-0.40	2.586
S on -OSiCH ₃ (O-CH ₃) ₂	-1.12	3.679
S on Cu(1 1 1)	-5.24	2.245
O ₂ on -OSiCH ₃ (O-CH ₃) ₂	-0.64	4.179
O ₂ on Cu(1 1 1)	-2.22	1.950
O on -OSiCH ₃ (O-CH ₃) ₂	-5.80	3.501
O on Cu(1 1 1)	-6.41	1.921

and $d_{adsorbate-surface}$ listed in Table 4. After geometry optimization, the $d_{adsorbate-surface}$ values for the O₂-OSiCH₃(O-CH₃)₂, O₂-Cu(1 1 1), O-OSiCH₃(O-CH₃)₂, and O-Cu(1 1 1) models changed to 4.179, 1.950, 3.501, and 1.921 Å, respectively, with E_{ads} values of -0.64, -2.22, -5.80, and -6.41 eV. In the O₂-OSiCH₃(O-CH₃)₂ and O₂-Cu(1 1 1) models, O₂ could only adsorb on the Cu(1 1 1) surface. In both the O-OSiCH₃(O-CH₃)₂ and O-Cu(1 1 1) models, the O atoms were stably adsorbed on the -OSiCH₃(O-CH₃)₂ and Cu(1 1 1). In the O-OSiCH₃(O-CH₃)₂ model, the O atom interacted strongly with the H atoms in CH₃ but did not penetrate the -OSiCH₃(O-CH₃)₂ layer to reach the Cu(1 1 1) surface.

As the primary component of the APPJ deposition film, -OSiCH₃(O-CH₃)₂ remained chemically stable and did not react with H₂S, H₂O, or their decomposition products. It did not react with O₂ but could attract O atoms. Fortunately, -OSiCH₃(O-CH₃)₂ effectively prevented O atoms from reaching the Cu(1 1 1) surface.

Based on the experimental tests and DFT simulation analyses above, the corrosion protection mechanism of the APPJ-deposited film for sintered nanoCu is illustrated. As shown in Fig. 15(a), under a high-voltage electric field, gases N₂, O₂, and Ar undergo collision ionization and Penning ionization, generating excited species (N₂^{*}, O₂^{*}, Ar^{*}, and

e⁻). These excited gas ions and electrons further induce the Penning ionization of HMDSO, given that the plasma has sufficient energy to break the chemical bonds (Si-O and Si-C) in HMDSO. HMDSO dissociation fragments, OSiCH₃ and OSi(CH₃)₃, can chemically bond to the surface of sintered nanoCu and further crosslink with other dissociation fragments to form a dense film primarily composed of Si-O₃ and Si-O₄. As shown in Fig. 15(b), a spherical clustered film forms during the APPJ treatment. Its microstructure and relatively low surface energy contribute to a reduction in the WCA. Additionally, the APPJ-deposited film serves as a barrier, isolating the sintered nanoCu surface from corrosive agents such as H₂S, O₂, NaCl, and H₂O, thereby protecting it from corrosion, as shown in Fig. 15(c).

4. Conclusion

This study proposed and validated a corrosion improvement method based on an APPJ-deposited film for sintered nanoCu materials. The physical state, composition, and water contact angle of the deposited film were experimentally measured. Subsequently, the protective effect of the deposited film on sintered nanoCu was confirmed through 384 h 2 ppm H₂S gas corrosion tests. Finally, the mechanism of the interaction between the deposited film and the Cu surface, as well as its protective mechanism against corrosion agents, was revealed using DFT. The key findings are as follows: (1) After APPJ treatment, a dense film was deposited on the surface of sintered nanoCu, with the main component being -Si-O₃. The film significantly improved the hydrophobicity of the sample, increasing the water contact angle from 101.0° to 134.8°. (2) After 384 h of exposure to 2 ppm H₂S-containing gas, the surface of sintered nanoCu without the deposited film formed a large amount of corrosion products, while the presence of the deposited film effectively prevented corrosion of the sintered nanoCu, and the film itself was not damaged by the corrosive gas. (3) During H₂S gas testing, the deposition film maintained the mechanical performances of the sintered nanoCu joint samples, while samples without the film experienced decreases in elastic modulus and hardness of 11 % and 16 %, respectively, following corrosion. (4) -OSiCH₃ and -OSi(CH₃)₃, as the dissociation fragments of

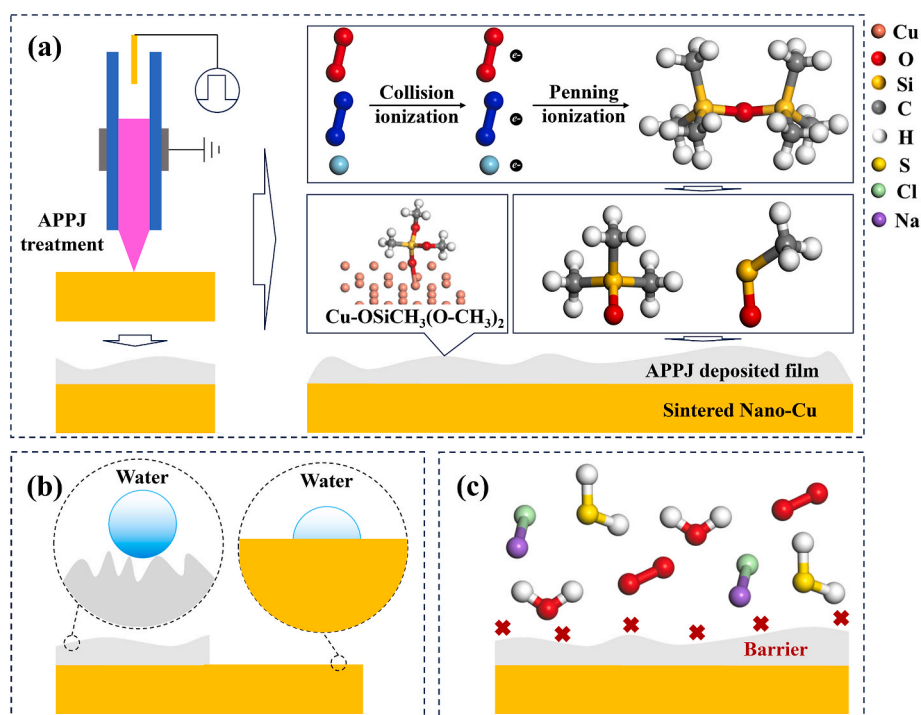


Fig. 15. Schematic representation of the corrosion protection mechanism: (a) formation of the APPJ-deposited film, (b) increased hydrophobicity, and (c) barrier effect against corrosive agents.

HMDSO, formed stable chemisorption with the sintered nanoCu surface, resulting in the formation of $-\text{OSi}(\text{CH}_3)(\text{O}-\text{CH}_3)_2$ fragments. $-\text{OSi}(\text{CH}_3)(\text{O}-\text{CH}_3)_2$ did not react with corrosion agents such as H_2S , O_2 , or H_2O and blocked the penetration of corrosion agents to the Cu surface. Generally, this study provides insights into a sintered nanoCu protection method using APPJ deposition, which is beneficial for the development of corrosion-resistant electronic devices in challenging environments.

CRedit authorship contribution statement

Jiajie Fan: Writing – original draft, Supervision, Project administration, Methodology, Funding acquisition, Conceptualization. **Wei Du:** Writing – review & editing, Investigation, Formal analysis, Data curation. **Wei Chen:** Writing – review & editing, Investigation, Formal analysis. **Junwei Chen:** Writing – review & editing. **Chenshan Gao:** Resources. **Liang Zhang:** Resources. **Xi Zhu:** Resources. **Huaiyu Ye:** Resources. **Chuan Chen:** Project administration, Funding acquisition. **Guoqi Zhang:** Supervision.

Declaration of competing interest

The authors declare that they have no known competing financial interests or personal relationships that could have appeared to influence the work reported in this paper.

Acknowledgments

This work was partially supported by National Natural Science Foundation of China (Grant No. 52275559) and State Key Laboratory of Environmental Adaptability for Industrial Products (Grant No. 2025EASKJ-003).

Data availability

Data will be made available on request.

References

- Y. Li, H. Mustafeez ul, A.B. Mirza, Y. Xie, S. Deng, S.S. Vala, F. Luo, X. Feng, S.V. J. Narumanchi, J.D. Flicker, State-of-the-art medium- and high-voltage silicon carbide power modules, challenges and mitigation techniques: a review, *IEEE Trans. Compon. Packag. Manuf. Technol.* 14 (12) (2024) 2177–2195.
- R. Jin, Z. Li, S. Liu, L. Sang, X. Chen, H. Linewih, Y. Zhong, F. He, Y. He, J. Han, A novel SiC vertical planar MOSFET design and optimization for improved switching performance, *Electronics* 13 (24) (2024) 4933.
- B. Hu, J. Wang, Z. Ke, C. Zhang, M. He, H. Yu, Y. Ding, Precise and fast real-time measurement of junction temperature in SiC power MOSFETs, *IEEE Trans. Ind. Appl.* 60 (6) (2024) 9134–9144.
- W.Y. Li, C.T. Chen, M. Ueshima, T. Kobatake, K. Sukanuma, Large area bare Cu-Cu interconnection using micro-Cu paste at different sintering temperatures and pressures, *Microelectron. Reliab.* 150 (2023) 115105.
- W. Chen, X. Liu, D. Hu, X. Liu, X. Zhu, X. Fan, G. Zhang, J. Fan, Unraveling the hydrogen sulfide aging mechanism on electrical-thermal-mechanical property degradation of sintered nanocopper interconnects used in power electronics packaging, *Mater. Des.* 238 (2024) 112702.
- W. Chen, X. Liu, Z. Yang, D. Hu, X. Liu, X. Zhu, X. Fan, G. Zhang, J. Fan, Insights into sulfur and hydrogen sulfide induced corrosion of sintered nanocopper paste: a combined experimental and ab initio study, *Mater. Des.* 240 (2024) 112876.
- O.O. Odeyemi, P.A. Alaba, Efficient and reliable corrosion control for subsea assets: challenges in the design and testing of corrosion probes in aggressive marine environments, *Corros. Rev.* 43 (1) (2025) 79–126.
- B. Wei, Z. Cai, M. Niu, J. Xu, B. Liao, T. Wu, C. Yu, C. Sun, Synergistic microbial interactions and electrochemical mechanisms driving microbiologically influenced corrosion in offshore platform produced seawater at 60 °C, *Corros. Sci.* 248 (2025) 112797.
- L. Feng, H. Shen, Y. Zhu, H. Gao, X. Yao, Insight into generation and evolution of sea-salt aerosols from field measurements in diversified marine and coastal atmospheres, *Sci. Rep.* 7 (1) (2017) 41260.
- Y. Wang, D. Xu, H. Yan, C.-F. Li, C. Chen, W. Li, Low-temperature copper sintering technology for power electronics packaging: a review, *J. Mater. Process. Technol.* 332 (2024) 118526.
- J. Becker, J. Pellé, S. Rioual, B. Lescop, N. Le Bozec, D. Thierry, Atmospheric corrosion of silver, copper and nickel exposed to hydrogen sulphide: a multi-analytical investigation approach, *Corros. Sci.* 209 (2022) 110726.
- X. Wang, Z. Yang, B. Wang, W. Chen, G. Zhang, J. Zhang, J. Fan, P. Liu, Effect of epoxy resin addition on properties and corrosion behaviour of sintered joints in power modules serviced offshore, *J. Mater. Res. Technol.* 25 (2023) 6593–6612.
- D. Li, Y. Mei, Y. Xin, Z. Li, P.K. Chu, C. Ma, G.-Q. Lu, Reducing migration of sintered ag for power devices operating at high temperature, *IEEE Trans. Power Electron.* 35 (12) (2020) 12646–12650.
- D. Wang, Y.-H. Mei, H. Xie, K. Zhang, K.S. Siow, X. Li, G.-Q. Lu, Roles of palladium particles in enhancing the electrochemical migration resistance of sintered nanosilver paste as a bonding material, *Mater. Lett.* 206 (2017) 1–4.
- C. Huang, L. Rao, H. Ling, A. Hu, M. Li, Research on the corrosion resistance of SAC305 solder added with Ag₃Sn and Cu₃Sn nanoparticles, in: 18th International Conference on Electronic Packaging Technology (ICEPT), 2017, pp. 712–715.
- Y. Lv, W. Yang, J. Mao, Y. Li, X. Zhang, Y. Zhan, Effect of graphene nano-sheets additions on the density, hardness, conductivity, and corrosion behaviour of Sn-0.7Cu solder alloy, *J. Mater. Sci. Mater. Electron.* 31 (1) (2020) 202–211.
- Y.-D. Han, L. Chen, H.Y. Jing, S.M.L. Nai, J. Wei, L.Y. Xu, Effect of Ni-coated carbon nanotubes on the corrosion behaviour of Sn-Ag-Cu solder, *J. Electron. Mater.* 42 (12) (2013) 3559–3566.
- R. Riva, C. Buttay, B. Allard, P. Bevilacqua, Migration issues in sintered-silver die attaches operating at high temperature, *Microelectron. Reliab.* 53 (9) (2013) 1592–1596.
- H. Tang, Z. Qu, L. Wang, H. Ye, X. Fan, G. Zhang, Correction: Liquid-phase exfoliated SnS as a semiconductor coating filler to enhance corrosion protection performance, *PCCP* 22 (21) (2020) 12321.
- S.-H. Liu, J.P. Trelles, C.-J. Li, C.-X. Li, H.-B. Guo, A review and progress of multiphase flows in atmospheric and low pressure plasma spray advanced coating, *Mater. Today Phys.* 27 (2022) 100832.
- A. Uricchio, F. Fanelli, Low-temperature atmospheric pressure plasma processes for the deposition of nanocomposite coatings, *Processes* (2021).
- J.A.C. Mendez, V.N.M. Escobedo, Y.M. Vong, J.D.J.P. Bueno, A review on atmospheric pressure plasma jet and electrochemical evaluation of corrosion, *Green Mater.* 10 (1) (2022) 11–22.
- G. Kalita, M.E. Ayhan, S. Sharma, S.M. Shinde, D. Ghimire, K. Wakita, M. Umeno, M. Tanemura, Low temperature deposited graphene by surface wave plasma CVD as effective oxidation resistive barrier, *Corros. Sci.* 78 (2014) 183–187.
- X. Zhu, X. Guan, L. Dai, X. Cui, J. Fan, Z. Fang, Improvement of electrical insulating properties for defective metal/epoxy resin interface in power modules by micro-plasma jet, *Appl. Surf. Sci.* 638 (2023) 158064.
- G.G. Jang, J. Jun, S. Yeom, M. Yoon, Y.F. Su, J. Wade, M.S. Stephens, J.K. Keum, Atmospheric pressure plasma treatment of magnesium alloy for enhanced coating adhesion and corrosion resistance, *Coatings* 13 (5) (2023) 897.
- X. Zhu, J. Xu, X. Guan, F. Li, K. Zhu, J. Huang, X. Cui, Z. Fang, Rapid evaluation of material surface modification by a dielectric barrier discharge based on fluorescence colouring and image processing technologies, *ACS Appl. Mater. Interf.* 14 (43) (2022) 49094–49108.
- D. Wang, L. Zhang, X.-T. Luo, C.-J. Li, MoSi₂ addition for high ablation resistance of dense ZrB₂-based composite coating prepared by very low-pressure plasma spraying, *Corros. Sci.* 209 (2022) 110800.
- P. Li, L. Li, W. Wang, W. Jin, X. Liu, K.W.K. Yeung, P.K. Chu, Enhanced corrosion resistance and hemocompatibility of biomedical NiTi alloy by atmospheric-pressure plasma polymerized fluorine-rich coating, *Appl. Surf. Sci.* 297 (2014) 109–115.
- L.L.G. Silva, F.V.P. Kodaira, P.V.M. Fagundes, A. Quade, K.G. Kostov, Study of organosilicon films deposited on SAE 1020 steel by atmospheric plasma jet for corrosion protection, *Braz. J. Phys.* 52 (4) (2022) 114.
- C. Regula, J. Ihde, U. Lommatsch, R. Wilken, Corrosion protection of copper surfaces by an atmospheric pressure plasma jet treatment, *Surf. Coat. Technol.* 205 (2011) S355–S358.
- S. Halder, M.A. Faridi, A. Rout, S.K. Nayak, I. Panda, T. Laha, Optimization of wetting behaviour in plasma-sprayed Fe-based amorphous/crystalline coatings resulting improved corrosion inhibition ability, *Surf. Coat. Technol.* 495 (2025) 131562.
- Z. Wang, X. Mao, Y. Lou, B. Zhao, L. Zhou, W. Jin, Y. Duan, Y. Yao, Y. Yu, H. Yu, F. Zhao, Z. Liu, Y. Wang, K. Zhang, W. Luo, Protective film on cerium metal through in-situ formation of a dense CeO₂ oxide layer using air plasma, *Chem. Eng. J.* 503 (2025) 158285.
- Y.-L. Kuo, K.-H. Chang, Atmospheric pressure plasma enhanced chemical vapor deposition of SiO_x films for improved corrosion resistant properties of AZ31 magnesium alloys, *Surf. Coat. Technol.* 283 (2015) 194–200.
- C. Jiang, Y. Wang, S. Wang, Y. Li, Y. Zou, J. Ouyang, D. Jia, Y. Zhou, Achieving high-efficiency electrically insulating ceramic layer formed on SiCp/Al composite by bipolar pulsed PEO for novel integrated strategy, *Surf. Coat. Technol.* 444 (2022) 128692.
- S.Y. Hsu, C.M. Tseng, J.H. Hsieh, Low-temperature atmospheric pressure plasma jets and their applications in the surface activation of some polymeric substrates for advanced electronic packaging, *Mater. Sci. Forum* 1112 (2024) 121–129.
- X. Liu, S. Li, J. Fan, J. Jiang, Y. Liu, H. Ye, G. Zhang, Microstructural evolution, fracture behaviour and bonding mechanisms study of copper sintering on bare DBC substrate for SiC power electronics packaging, *J. Mater. Res. Technol.* 19 (2022) 1407–1421.
- W. Chen, S. Feng, X. Liu, D. Hu, X. Liu, X. Zhu, Q. Yao, X. Fan, G. Zhang, J. Fan, Rapid on-site nondestructive surface corrosion characterization of sintered nanocopper paste in power electronics packaging using hyperspectral imaging, *Microelectron. Reliab.* 162 (2024) 115508.
- X. Cui, L. Li, Z. Xu, X. Zhu, S. Akram, Z. Fang, Enhanced surface performance of insulating ceramic by plasma polymerization with nanosecond-pulse dielectric

- barrier discharge: insight into the effect of the repetition frequency, *J. Vac. Sci. Technol. A* 42 (4) (2024).
- [39] C. Zheng, B. Guo, T. Lu, X. Zhu, B. Xia, B. Yang, Z. Yang, S. Lishik, A. Chernyakov, J. Xiong, J. Fan, Enhanced highly thermal-humidity reliability of (Sr,Ca)AlSiN₃:Eu²⁺ phosphors via rapid plasma-assisted silica surface coating, *Opt. Exp.* 33 (3) (2025) 4940–4956.
- [40] S. Duan, I.Y. Zhang, Z. Xie, X. Xu, Identification of water hexamer on Cu(111) surfaces, *J. Am. Chem. Soc.* 142 (15) (2020) 6902–6906.
- [41] J.H. Chang, A. Huzayyin, K. Lian, F. Dawson, Interaction of H₂O and H₂S with Cu (111) and the impact of the electric field: the rotating & translating adsorbate, and the rippled surface, *PCCP* 17 (1) (2015) 588–598.
- [42] R. Zhang, H. Liu, J. Li, L. Ling, B. Wang, A mechanistic study of H₂S adsorption and dissociation on Cu₂O(111) surfaces: thermochemistry, reaction barrier, *Appl. Surf. Sci.* 258 (24) (2012) 9932–9943.